

Band structures and optical properties of $\text{Ga}_{1-x}\text{In}_x\text{As}$ quantum wires grown by strain-induced lateral ordering

Liang-Xin Li and Yia-Chung Chang

*Department of Physics and Materials Research Laboratory
University of Illinois at Urbana-Champaign, Urbana, Illinois 61801*
(August 13, 2018)

Band structures and optical matrix elements of strained multiple quantum-wires (QWR's) are investigated theoretically via the effective bond-orbital model, which takes into account the effects of valence-band anisotropy and the band mixing. In particular, the $\text{Ga}_{1-x}\text{In}_x\text{As}$ QWR's grown by strain-induced lateral ordering (SILO) are considered. Recently, long wavelength $\text{Ga}_{1-x}\text{In}_x\text{As}$ QWR lasers have been fabricated via a single step molecular beam epitaxy technique which uses the SILO process.[1] Low threshold current and high optical anisotropy have been achieved. Multi-axial strains [combinations of biaxial strains in the (001) and (110) planes] for QWR's are considered, Our calculated anisotropy in optical matrix elements (for light polarized parallel versus perpendicular to the QWR's axis) is in good agreement with experiment. We also find that the strain tends to increase the quantum confinement and enhance the anisotropy of the optical transitions.

I. INTRODUCTION

$Ga_xIn_{1-x}As$ is one of the most important ternary III-V compound semiconductors. Its bandgap covers both the 1.3 and 1.55 μm range, which are the preferred wavelengths in long distance fiber communications[1,2]. However, long-wavelength photonic devices based on lattice-matched $Ga_{0.47}In_{0.53}As/InP$ heterostructures suffer from strong Auger recombination and intervalence band absorption processes[7-10]. Recently, to improve the performance of long-wavelength semiconductor lasers, long wavelength($\sim 1.55\mu m$) $Ga_xIn_{1-x}As$ quantum-wire (QWR) lasers have been grown by a single step molecular beam epitaxy technique[1]. It is found that the QWR laser structures are a promising choice because of the many predicted benefits, such as higher gain, reduced temperature sensitivity, higher modulation bandwidths, and narrower spectral linewidths[2]. Short-period superlattices (SPS) in the direction perpendicular to the growth direction can be formed via the strain-induced lateral-layer ordering (SILO) process[1,2]. A quantum wire heterostructure can then be created by simply utilizing this SPS structure as the quantum well region in a conventional quantum heterostructure. Besides the self-assembled lateral ordering, it is believed that the strain also plays a key role[2] in the temperature stability and high anisotropy for the QWR laser structure. Recent studies indicate that the use of the strained-layer quantum wire heterostructure has advantages of high-quality interfaces and band-gap tuning which are independent of the lattice constant of the constituent materials[3,4,6]. Furthermore, much work has been undertaken which predicts that by using strained-layer superlattice to form the active region of a quantum-wire laser, the threshold current can be decreased by one order of magnitude, and the optical loss due to intervalence-band absorption and Auger recombination will also be greatly reduced[1,2,7-10]. Also, the temperature sensitivity is reduced by a order of magnitude compared with strain-free structures[2]. A typical temperature sensitivity of the lasing wavelength is($\sim 5\text{\AA}/^{\circ}C$) for the usual GaInAs/InP lasers. By using a distributed-feedback structure, the temperature dependence of the lasing wavelength is reduced to $1\text{\AA}/^{\circ}C$ [2]. With this strained GaInAs QWR, the dependence is smaller than $0.1\text{\AA}/^{\circ}C$ [2]. It should be an important improvement on the current technology in fabricating the long wavelength lasers for fiber communication. In this paper we study the effects of multi-axial strain on the electronic and optical properties of the QWR structures grown via the SILO process. Through this study, we can gain a better understanding of the strain engineering of QWR structures suitable for the application of fiber-optical communication.

In the experiment performed by Chou et al[1], the QWR active region is created *in situ* by the SILO process within the $(GaAs)_2/(InAs)_{2.2}$ SPS regions. The SILO process generates a strong Ga/In lateral composition modulation and creates In-rich $Ga_xIn_{1-x}As$ lateral QWs in the [110] direction. By sandwiching the In composition modulated layer (with x varying from 0.3 to 0.7) between $Al_{0.24}Ga_{0.24}In_{0.52}As$ barrier layers, a strained QWR heterostructure is formed[1,2]. The model QWR structure considered in the present paper is depicted in Figure.1. The central region consists of the In composition modulated $Ga_xIn_{1-x}As$ layer (A/B/A/B...), in which the A strip is Ga-rich while the B strip is In-rich. The lateral period is $L_2 = L_2^A + L_2^B$. In our calculation, we consider $L_2^A = L_2^B = 50\text{\AA}$ and $L_{\perp}^B = L_{\perp}^W = 50\text{\AA}$. We consider two cases of composition modulation. In case one, the Ga composition changes abruptly with $x = 0.6$ (or 0.7) in strip A and $x = 0.4$ (or 0.3) in strip B. In case two, x varies sinusoidally from 0.6 (or 0.7) at the center of strip A to 0.4 (or 0.3) at the center of strip B (with $x = 0.5$ at the border between A and B strips).

II. THEORETICAL APPROACH

The method used in this paper for calculating the strained quantum well band structure is based on the effective bond-orbital model (EBOM). A detailed description of this method without the effect of strain has been published elsewhere[5]. Here we give a brief account of the method and discuss the effect of strains. The effective bond-orbital model employed here is a tight-binding-like model which includes nearest-neighbor interactions among bond orbital residing on an fcc lattice. The version of the EBOM used in this calculations describes the coupling between the upper four spin-3/2 valence bands and the lowest two s-like conduction bands. For our QWR system, the split-off bands are ignored since the spin-orbital splitting is large. A bond orbital is defined to be the proper linear combination of the two atomic orbitals within a zinc-blende crystal which best describes the states near the center of the Brillouin zone. The parameters that appear in the theory are given by a correspondence which is made by requiring that the Hamiltonian in the bond-orbital basis, when written for the bulk material and expanded to the second order in \mathbf{k} , agree with the Luttinger-Kohn expression. For interactions across heterojunctions, we take the average of the matrix elements for the two bulk materials. EBOM has been successfully applied to the calculation of electronic states of superlattices[5], strained-layer superlattices [6,19], semiconductor quantum wires[15] and dots[17], and impurity levels in quantum dots[17] and quantum wells[17]. Here, we apply it to this multi-axially strained QWR structures.

We solve the QWR electronic states according to a procedure similar to that described in [15]. We first calculate the band structure of a superlattice(SL) with M bilayers of $Ga_xIn_{1-x}As$ (the well material) and N bilayers of $Al_{0.24}Ga_{0.24}In_{0.52}As$ (the barrier material) using the slab method. The superlattice period is $L_{\perp} = L_{\perp}^B + L_{\perp}^W =$

$(M+N)a/2$, where a is the lattice constant. For a sufficiently large value of the barrier thickness (we used $L_{\perp}^B = 50\text{\AA}$) the QW's are essentially decoupled and we ignore the dependence on the wave number in the growth direction, taking $k_z = 0$. The SL eigenstates with $k_z = 0$ are denoted by $|k_1, \bar{k}_2, n\rangle$, i.e.,

$$H^{SL}|k_1, \bar{k}_2, n\rangle = E_n(k_1, \bar{k}_2)|k_1, \bar{k}_2, n\rangle \quad (1)$$

where H^{SL} is the Hamiltonian for the $Ga_yIn_{1-y}As/Al_{0.24}Ga_{0.24}In_{0.52}As$ SL ($y = 0.6$ or 0.7), where k_1 and k_2 are the two components of the SL in-plane wave vector along and perpendicular to the QWR axis, respectively. k_1 is a good quantum number for the QWR array, while \bar{k}_2 is not. The QWR wave function is a linear combination of SL wave functions with the same k_1 but with values of \bar{k}_2 differing by $2\pi/L_2$. We define k_2 to be the wave number of the QWR array in the $[110]$ direction, and we can write $\bar{k}_2 = k_2 + 2\pi\zeta/L_2$ with $\zeta = 0, 1, 2, \dots, m$, where $m = L_2/a_2$ with $a_2 = a/\sqrt{2}$. The QWR Hamiltonian is $H^{QWR} = H^{SL} + H'$, where $H' = H_{Ga_xIn_{1-x}As} - H_{Ga_yIn_{1-y}As}$ is treated as a perturbation. The Hamiltonian matrix for QWR

$$M(n, \zeta|n', \zeta') = \langle k_1, k_2 + 2\pi\zeta'/L_2 | H^{QWR} | k_1, k_2 + 2\pi\zeta/L_2, n \rangle \quad (2)$$

is then diagonalized in the basis consisting of SL eigenstates. The basis is truncated to reduce the computer time, thus making the method a variational one. The subbands closest to the band edge are converged to within 0.1 meV. The size of the Hamiltonian matrix, originally given by the number of sites in a QWR supercell times the number of coupled bands, is now reduced to the number of SL states necessary to give accurate results for the QWR of concern. In our case, this number needed to get well converged results for the two uppermost pair of valence subbands is around 200. However, we have used ~ 800 basis states in order to ensure the accuracy of the deeper lying states for all calculations in this present paper. The effect of lateral intermixing of Ga and In is accounted for by using the virtual-crystal approximation. Bond-orbital parameters for the inter-diffused materials are obtained by linearly interpolating between the values of the parameters for the pure materials. The optical parameters in these expressions are determined by requiring that the optical matrix elements between bulk states obtained by EBOM be identical to those obtained in the $\mathbf{k} \cdot \mathbf{p}$ theory up to second order in \mathbf{k} [15].

The effect of strain is included by adding a strain Hamiltonian H^{st} to the EBOM effective Hamiltonian[6,10,16]. The matrix elements of H^{st} in the bond-orbital basis can be obtained by the deformation-potential theory of Bir and Pikus[16]. Here, we consider the combination of two bi-axial strains, one in the (001) plane (due to the lattice mismatch at the interfaces between GaInAs and AlGaInAs) and the other in the (110) plane (due to the Ga composition modulation). The resulting strains in the SL layers consist of both hydrostatic and uniaxial components. For case 1 (Ga composition changes abruptly from region A to region B), the lattice constant of the strained layers in the $[001]$ direction (\tilde{a}_{001}) is given by minimizing the free energy of the fcc system due to strain[11]:

$$\begin{aligned} F = & \frac{1}{2}C_{11}^A(\epsilon_{11A}^2 + \epsilon_{22A}^2 + \epsilon_{33A}^2)L_2^A \\ & + C_{12}^A(\epsilon_{11A}\epsilon_{22A} + \epsilon_{22A}\epsilon_{33A} + \epsilon_{11A}\epsilon_{33A})L_2^A \\ & + \frac{1}{2}C_{11}^B(\epsilon_{11B}^2 + \epsilon_{22B}^2 + \epsilon_{33B}^2)L_2^B \\ & + C_{12}^B(\epsilon_{11B}\epsilon_{22B} + \epsilon_{22B}\epsilon_{33B} + \epsilon_{11B}\epsilon_{33B})L_2^B, \end{aligned} \quad (3)$$

where L_2^A (L_2^B) is the lateral layer thickness and ϵ_{ijA} (ϵ_{ijB}) is the strain tensor in the Ga-rich (In-rich) region. C^A 's (C^B 's) are the elastic constants for the Ga-rich (In-rich) materials. Here we have used a rotated Cartesian coordinates in which $x' = [1\bar{1}0]$, $y' = [110]$, and $z' = [001]$. A constraint $\tilde{a}_{\parallel}^A = \tilde{a}_{\parallel}^B = a_{InP} = a_{AlInGaAs}$ has been imposed to keep the $Al_{0.24}Ga_{0.24}In_{0.52}As$ barrier strain free, since it is lattice-matched to the InP substrate[1,2], where $\tilde{a}_{\parallel}^{\alpha}$ is the in-plane strained lattice constant (perpendicular to $[001]$ axis) for material α . The multi-axial strain caused by the lattice-mismatch in both (001) and (110) planes is simply

$$\epsilon_{11\alpha} = \epsilon_{22\alpha} = \frac{\tilde{a}_{\parallel}^{\alpha} - a_{\alpha}}{a_{\alpha}}, \quad (4)$$

where a_A (a_B) is the unstrained lattice constant of $Ga_xIn_{1-x}As$ ($Ga_{1-x}In_xAs$) ($x = 0.6$ for case 1) and

$$\epsilon_{33\alpha} = \frac{\tilde{a}_{001} - a_{\alpha}}{a_{\alpha}} \quad (5)$$

with $\epsilon_{ij}^{\alpha} = 0$ for $i \neq j$.

The minimization procedure leads to

$$\tilde{a}_{001} = -\frac{1}{2} \frac{C_{11}^A L_2^A / a_A^2 + C_{11}^B L_2^B / a_B^2}{(C_{12}^A \epsilon_{\parallel}^A L_2^A / a_A + C_{12}^B \epsilon_{\parallel}^B L_2^B / a_B) + (C_{11}^A L_2^A / a_A + C_{11}^B L_2^B / a_B)}, \quad (6)$$

which is the strained lattice constant in the [001] direction.

Due to symmetry, the multi-axial strain tensor is diagonal in the $x'y'z'$ coordinates, which leads to a diagonal strain Hamiltonian

$$H^{st} = \begin{pmatrix} -\Delta V_H + D_1 & 0 & 0 \\ 0 & -\Delta V_H + D_2 & 0 \\ 0 & 0 & -\Delta V_H + D_3 \end{pmatrix}, \quad (7)$$

where

$$\Delta V_H = (a_1 + a_2)(\epsilon_{11} + \epsilon_{22} + \epsilon_{33}), \quad D_1 = b(2\epsilon_{11} - \epsilon_{22} - \epsilon_{33}), \quad D_2 = b(2\epsilon_{22} - \epsilon_{11} - \epsilon_{33}), \quad D_3 = b(2\epsilon_{33} - \epsilon_{22} - \epsilon_{11}),$$

The strain potential on the s states is given by[6]

$$\Delta V_c = c_1(\epsilon_{11} + \epsilon_{22} + \epsilon_{33}),$$

The strain Hamiltonian in the bond-orbital basis $|JM\rangle$ can be easily found by using the coupling constants[5], i.e,

$$\langle JM | H^{st} | J' M' \rangle = \sum_{\alpha, \alpha', \sigma} C(\alpha, \sigma; J, M)^* C(\alpha', \sigma; J', M') H_{\alpha\alpha'}^{st} \quad (8)$$

The elastic constants C_{12} and C_{11} for GaAs, InAs and AlAs can be found in Ref. [12,18]. The deformation potentials a_1 , a_2 , b , c_1 can be found in Ref.[20,21]. The linear interpolation and virtual crystal approximation is used to obtain the corresponding parameters for the GaInAs and AlGaInAs.

After rotating back to the original Cartesian coordinates, the final results for the strain Hamiltonian in the bond-orbital basis $|JM\rangle$ is

$$H^{st} = \begin{pmatrix} \Delta V_c & 0 & 0 & 0 & 0 & 0 \\ 0 & \Delta V_c & 0 & 0 & 0 & 0 \\ 0 & 0 & -V_H + A & 0 & B/\sqrt{12} & 0 \\ 0 & 0 & 0 & -V_H + C & 0 & B/\sqrt{12} \\ 0 & 0 & B/\sqrt{12} & 0 & -V_H + C & 0 \\ 0 & 0 & 0 & B/\sqrt{12} & 0 & -V_H + A \end{pmatrix} \quad (9)$$

with

$$A = \frac{D_3 + 0.5(D_1 + D_2)}{2}, \quad B = \frac{(D_1 + D_2)}{2} - D_3, \quad C = \frac{2.5(D_1 + D_2) + D_3}{6}.$$

One can see non-diagonal terms arise due to the rotation, which will cause additional mixing and optic transitions between different valence bands.

The above strain Hamiltonian is derived for case one only, where the Ga composition (x) changes abruptly from region A to region B. For case two, x varies continuously from x_m to $1-x_m$ ($x_m = 0.6$ or 0.7). In this case, we shall first calculate the strain Hamiltonian for the abrupt case to get $H_{x_m}^{st}$ and $H_{1-x_m}^{st}$, using Eq. (8). We then obtain the strain Hamiltonian at any atomic layer with Ga composition x via a linear interpolation between $H_{x_m}^{st}$ and $H_{1-x_m}^{st}$. This is consistent in spirit with the virtual crystal approximation we have used for obtaining the interaction parameters in EBOM.

III. RESULTS AND DISCUSSIONS

In Figure 2, we show a schematic diagram indicating the alignment between band edges of the constituent materials for QWR in case 1 (square profile) with and without the effect of strain. All energies are measured with respect to the bulk InAs valence band edge. This diagram is useful in understanding the quantum confinement effect on the QWRs

considered here. From Figure 2, we notice that the strain [in particular, the one in the (110) plane] has a significant effect on the band alignment. Take Figure 2(a) for example, without strain (solid lines) the conduction (valence) band of $\text{Ga}_{0.4}\text{In}_{0.6}\text{As}$ is below (above) that of $\text{Ga}_{0.6}\text{In}_{0.4}\text{As}$ by 247 meV (14 meV). With strain (dotted lines), the situation is reversed and the conduction (valence) band of $\text{Ga}_{0.4}\text{In}_{0.6}\text{As}$ is above (below) that of $\text{Ga}_{0.6}\text{In}_{0.4}\text{As}$ by 312 meV (76 meV); thus, both electrons and holes will be confined in the Ga-rich region of the QWR. We found that about 80 % of these changes are caused by the strain in the (110) plane, since there is a stronger lattice mismatch between $\text{Ga}_{0.6}\text{In}_{0.4}\text{As}$ and $\text{Ga}_{0.4}\text{In}_{0.6}\text{As}$ compared with that between $\text{Ga}_{0.6}\text{In}_{0.4}\text{As}$ and $\text{Al}_{0.24}\text{Ga}_{0.24}\text{In}_{0.52}\text{As}$ (or InP).

The strain also causes a splitting between the heavy-hole (HH) and light-hole (LH) bands with the LH band lying above the HH band. However, the splitting is rather small, about 3 meV in $\text{Ga}_{0.6}\text{In}_{0.4}\text{As}$. When the confinement effect due to the barrier material ($\text{Al}_{0.24}\text{Ga}_{0.24}\text{In}_{0.52}\text{As}$) is included, the HH band again lies above the LH band, due to the difference in the effective masses along the growth direction (z). The dash-dotted lines in Figure 2(a) indicate the superlattice band edges of $50\text{\AA}\text{Ga}_{0.6}\text{In}_{0.4}\text{As}$ (or $\text{Ga}_{0.4}\text{In}_{0.6}\text{As}$) sandwiched between $50\text{\AA}\text{Al}_{0.24}\text{Ga}_{0.24}\text{In}_{0.52}\text{As}$ barriers. The difference in superlattice band edges (dash-dotted lines) between $\text{Ga}_{0.6}\text{In}_{0.4}\text{As}$ and $\text{Ga}_{0.4}\text{In}_{0.6}\text{As}$ determines the degree of lateral quantum confinement in the QWR. For the present case, the conduction-band offset is 252 meV and the valence-band (for HH only) offset is 52 meV, as far as the lateral confinement is concerned. Both offsets are large enough to give rise to strong lateral confinement for electrons and holes in the Ga-rich region.

Figure 3 shows the near zone-center valence subband structures of square-shaped QWRs with the multi-axial strain with (a) Ga composition (x) changing abruptly from 0.6 in region A to 0.4 in region B and (b) Ga composition (x) changing abruptly from 0.7 in region A to 0.3 in region B. To compare with experiment[1,2], we choose material parameters appropriate for temperature at 77K[12]. All subbands are two-fold degenerate due to the Kramer's degeneracy and they are labeled according to the characters of their underlying Bloch functions at the zone-center: HH for heavy hole and LH for light-hole (only the confined subbands are labeled). The conduction subbands are approximately parabolic as usual with a zone-center subband minimum equal to 826 meV in (a) and 707 meV in (b) (not shown in the figure). This gives an energy gap 860 meV for the ($x=0.6/0.4$) QWR array and 708 meV for the ($x=0.7/0.3$) QWR array.

The observed C1-HH1 excitonic transition is at 735 meV (or $1.65\mu\text{m}$) for the QWR[1,2] at 77K. In comparing the band gaps with the experiment, one should also take into account the exciton binding energy which is around 20 meV for this size of QWR. Thus, the theoretical result for the ($x=0.7/0.3$) QWR array is in closer agreement with experiment, but about 50 meV too low.

Comparing the band structures in both k_1 ($[1\bar{1}0]$) and k_2 ($[110]$) directions, we noticed an apparent anisotropy in the energy dispersion. The dispersions in the k_2 direction for the five uppermost (confined) valence bands are rather small, indicating strong lateral confinement. We observe strong anti-crossing effect between the HH1/HH2 and LH1 subband at k_1 near 0.02\AA^{-1} similar to what happens in a quantum well²². Here the HH2 subband of the QWR corresponds to the $[110]$ zone-folded part of the HH1 subband of the quantum well (the envelope function has odd parity in the $[110]$ direction but even parity in the $[1\bar{1}0]$ direction).

The subbands in Figure 3(b) have less dispersion in the k_2 direction compared with those in Figure 3(a) as a result of stronger lateral confinement. This is caused by the larger band discontinuities in the $x=0.3/0.7$ case (versus the $x=0.4/0.6$ case) as can be seen by comparing band alignments shown in Figure 2.

Figure 4 shows the near zone-center valence subband structures of a QWR with a sinusoidal lateral modulation with Ga composition (x) varying as the position (y') in the $[110]$ direction between two extreme values x_m and $1 - x_m$, i.e.

$$x(y') = 0.5 + (0.5 - x_m)\sin(2\pi y'/L_2)$$

for $x_m = 0.4$ and (b) $x_m = 0.3$. In this case, the Hamiltonian including the multi-axial strain is calculated with a linear extrapolation between the Hamiltonians for the maximum and minimum Ga composition, i.e.

$$H_{\text{Ga}_x\text{In}_{1-x}\text{As}}^{\text{st}} = fH_{\text{Ga}_{x_m}\text{In}_{1-x_m}\text{As}} + (1 - f)H_{\text{Ga}_{1-x_m}\text{In}_{x_m}\text{As}},$$

where $x_m = 0.4$ or 0.3 and f is determined by comparing the Ga composition on both sides of the equation

$$x = x_m f + (1 - x_m)(1 - f),$$

or $f = (1 - x_m - x)/(1 - 2x_m)$.

The conduction band minimum (not shown) is 850 meV (757 meV) for the case $x_m = 0.4$ ($x_m = 0.3$), which corresponds to a band gap of 889 meV (767 meV). Subtracting the exciton binding energy (~ 20 meV) from the band gap, we found that the $x_m = 0.3$ case is in fairly good agreement with the observed excitonic transition energy of 735 meV. The band gaps of QWR's with the sinusoidal profile are consistently larger (by about 30-50 meV) than the corresponding QWR's with the square-profile (with the same extreme values of Ga composition). The sinusoidal

variation in Ga composition gives rise to more energy, since the well region contains more materials with band gap higher than the minimum in comparison with the square-profile. Furthermore, the lateral strain is reduced (less mismatch on the average) which also tend to increase the band gap.

Comparing Figure 4 with Figure 3, we notice that the spacing between HH1 and HH2 is substantially larger for the sinusoidal profile than for the square profile. This can be understood by the following argument. The envelope function for the HH2 state is more spread out than that for the HH1 state, thus its energy is increased more in the sinusoidal profile (with higher probability being in materials with higher band gap) compared with the square profile.

Next we discuss the optical properties of QWR's. Since the QWR states can be qualitatively viewed as the zone-folded states of the superlattice (SL) states (the zeroth-order states) via the lateral confinement, it is instructive to examine the optical matrix elements of the SL case. Figure 5 shows the squared optical matrix elements of the (50Å/50Å) Ga_{0.7}In_{0.3}As/Al_{0.24}Ga_{0.24}In_{0.52}As superlattice for the HH1-C1 and LH1-C1 transitions versus the wave vector k_2 . The solid and dashed lines are for the polarization vector along the k_1 ([1 $\bar{1}$ 0]) and k_2 ([110]) directions, respectively. We note that the optical matrix elements are isotropic in the x - y plane at the zone-center, while they become anisotropic at finite values of k_2 . At the zone center, the HH state consists of Bloch states with atomic character ($x' + iy'$) \uparrow ($|J, M \rangle = |3/2, 3/2 \rangle$), while the LH state consists of Bloch states with atomic character ($x' - iy'$) $\uparrow + 2z \downarrow$ ($|J, M \rangle = |3/2, -1/2 \rangle$); thus, the corresponding optical transitions (to an s-like conduction band state) are isotropic in the x - y plane. Here $x'(y')$ is the coordinate along the $k_1(k_2)$ direction. For finite k_2 , the HH and LH characters are mixed, with the HH state consisting of more x' -character than y' -character, thus in favor of the polarization vector parallel to the k_1 direction. Note that the HH (LH) band tends to have an atomic character with polarization perpendicular (parallel) to the direction of wave vector. This is a direct consequence of the fact that the ($pp\pi$) interaction is weaker than the ($pp\sigma$) interaction in a tight-binding model. Since QWR states are derived from the SL states with finite values of k_2 , we expect the optical matrix elements of QWR to be anisotropic in the x - y plane as well.

Figures 6 and 7 show the squared optical matrix elements versus wave vectors of the corresponding QWR's considered in Figures 3 and 4, respectively. The solid and dashed lines are for the polarization vector along the k_1 ([1 $\bar{1}$ 0]) (parallel to the wire) and k_2 ([110]) (perpendicular to the wire) directions. The optical matrix elements together with the subband structures discussed above provide the essential ingredients for understanding the optical transitions observed in the photoluminescence (PL) measurements. In all figures the optical transitions considered are from the topmost three valence subbands to the lowest conduction subband: HH1-C1, HH2-C1, and LH1-C1. These curves were obtained by summing the contributions of two degenerate subbands (due to Kramer's degeneracy) for the initial and final states. To compare with experimental (PL) results, we concentrate on the HH1-C1 transition.

From Figures 6 and 7, we found for the parallel polarization (solid lines), the squared optical matrix element for the HH1-C1 transition has a maximum at the zone center with a value near 25 eV and remains close to this maximum value for all finite k_2 and with $k_1 = 0$. For the perpendicular polarization, the HH1-C1 transition is very small for finite k_2 and $k_1 = 0$. This means that the wave function of the HH1 state has mostly x' character (and some z character). Thus, we conclude that the strong lateral confinement forces the wave function of the HH1 state with $k_1 = 0$ to change from the $x' + iy'$ character (in the SL case) into mostly x' character. At finite k_1 , the character of the HH1 state gradually changes back toward the $x' + iy'$ character and the optical transition becomes almost isotropic when k_1 is comparable to zone-boundary value of $k_2(\pi/L_2)$, and finally turns into mostly y' character as k_1 becomes much larger than (π/L_2) . The anti-crossing behavior of the HH1/HH2 subbands with the LH1 subband further complicates the whole picture at $k_1 \approx 2\text{\AA}^{-1}$.

The HH2-C1 transition has zero optical strength at the zone center for both polarizations. This is expected, since the HH2 state has odd parity in the envelope function, which leads to forbidden transition at the zone center. The symmetry restriction is relaxed as the wave vector deviate from zero. The LH1-C1 transition has large optical strength (around 17 eV) for the perpendicular polarization and very weak strength (around 1 eV) for the parallel polarization at the zone center. This indicates that the LH1 states consists of mostly y' character. So the strong lateral confinement forces the the wave function of the LH1 state with $k_1 = 0$ to change from the $x' - iy'$ character (in the SL case) into mostly y' character. In other words, the HH1 state (with pure $x' + iy'$ character) and LH1 state (with pure $x' - iy'$ character) in the SL case are mixed thoroughly by the lateral confinement in QWR to produce a predominantly x' state (HH1) and a predominantly y' (LH1) state. Note that all these states consist of appreciable z character, which will appear in the optical transition with z polarization.

To calculate the anisotropy, we integrate the squared optical matrix element over range of k_1 corresponding to the spread of exciton envelope function in the k_1 space. The exciton envelope function is obtained by solving the 1D Schrödinger equation for the exciton in the effective-mass approximation

$$\left[-\frac{\hbar^2}{2\mu}\left(\frac{\partial}{\partial x'}\right)^2 + V_X(x')\right]F(x') = E_X F(x'), \quad (10)$$

where μ is the exciton reduced mass ($\approx 0.037m_0$) and $V_X(x')$ is the effective 1D exciton potential given by²³

$$V_X(x') = \frac{e^2}{\epsilon_0|x'|}(1 - e^{-\beta|x'|}).$$

The parameter β is obtained by extrapolation from the values given in Table V of Ref.²³. For a 50Å quantum wire, we obtain $\beta = 0.07\text{\AA}^{-1}$. Eq. (10) is solved numerically, and the exciton envelope function in k_1 space is obtained via the Fourier transform of $F(x')$. The exciton binding energy obtained is 23 meV. We found that the ratio of the averaged optical strength for the HH1-C1 transition for the parallel to perpendicular component of the polarization vector is 2.65 (4.04) for the $x = 0.4/0.6$ ($x = 0.3/0.7$) QWR with square profile, and 2.86 (7.19) for the $x_m = 0.4$ ($x_m = 0.3$) QWR with sinusoidal profile. The $x_m = 0.3$ case shows stronger optical anisotropy than the $x_m = 0.4$ case, indicating that the stronger lateral confinement leads to stronger optical anisotropy as expected. Experimentally, the optical anisotropy is found to be around 2-4. So, our results are consistent with experiment.

IV. CONCLUSION

We have calculated the band structures and optical matrix elements for the strained QWR grown by the SILO method. The effect of multi-axial strain on the valence subbands and optical matrix elements is discussed. Our theoretical studies provide the explanation of the anisotropy in optical matrix elements of these QWR's observed experimentally. We find that the biaxial strain due to the lattice mismatch between the Ga-rich and In-rich regions is most dominant. It tends to increase the lateral confinement in the QWR and enhances the anisotropy of the optical transitions which may be useful for certain applications in optical communication. We also calculated the effect of lateral composition modulation on the band structures and optical properties and find that it increases the band gaps and reduces the optical anisotropy. From the above discussions, we can use the theoretical predictions to guide the engineering design of QWR optical devices. The temperature effect will be incorporated in our future studies in order to understand the temperature stability of the optical transitions of QWR's grown by the SILO method.

ACKNOWLEDGEMENTS

This work was supported in part by the National Science Foundation (NSF) under Grant No. NSF-ECS96-17153. We would like to thank K. Y. Cheng and D. E. Wohlert for fruitful discussions and for providing us with the detailed experimental data of the QWR structures considered here.

- ¹ S.T. Chou, K. Y. Cheng, L. J. Chou, and K. C. Hsieh, Appl. Phys. Lett. **17**, 2220 (1995); J. Appl. Phys. **78** 6270, (1995); J. Vac. Sci. Tech. B **13**, 650 (1995); K. Y. Cheng, K. C. Hsien, and J. N. Baillargeon, Appl. Phys. Lett. **60**, 2892 (1992).
- ² D. E. Wohlert, S. T. Chou, A. C. Chen, K. Y. Cheng, and K. C. Hsieh, Appl. Phys. Lett. **17**, 2386 (1996).
- ³ J. W. Matthews and A. E. Blakeslee, J. Cryst. Growth **27**, 118 (1974).
- ⁴ G. C. Osbourn, Phys. Rev. **B27**, 5126 (1983).
- ⁵ Y. C. Chang, Phys. Rev. **B37**, 8215 (1988).
- ⁶ Mau-Phon Houng and Y.C Chang, J. Appl. Phys. **65**, 3096 (1989).
- ⁷ P. L. Gourley, J. P. Hohimer, and R. M. Biefeld, Appl. Phys. Lett. **47**, 552 (1985).
- ⁸ A. R. Adams, Electron. Lett. **22**, 249 (1986).
- ⁹ E. Yablonovitch and E. O. Kane. IEEE J. Lightwave Technol. LT-4, 504 (1986).
- ¹⁰ G. P. Agrawa and N. K. Dutta, Long Wavelength Semiconductor Lasers, 2nd ed. (Van. Nostrand Reinhold, New York, 1993) Chap.7.
- ¹¹ G. L. Bir and G. E. Pikus, Symmetry and Strain Induced Effects in Semiconductors (Halsted, United Kingdom, 1974); L.D. Landau and E. L. Lifshitz, Theory of Elasticity (Addison-Wesley Publishing Company Inc, Reading, Massachusetts, USA, 1970).
- ¹² S. Adachi, J. Appl. Phys. **53**, 8775 (1982).
- ¹³ H. Mathieu, P. Meroe, E. L. Amerziane, B. Archilla, J. Camassel, and G. Poiblaud, Phys. Rev. **B19**, 2209 (1979); S. Adachi and C. Hamaguchi, Phys. Rev. **B19**, 938 (1979).

- ¹⁴ J. M. Hinckley and J. Singh, Phys. Rev. B**42**, 3546 (1990).
- ¹⁵ D. S. Citrin and Y. C. Chang, Phys. Rev. B**43**, 11703 (1991).
- ¹⁶ G. C. Osbourn, J. Appl. Phys. **53**, 1586 (1981).
- ¹⁷ G. T. Enievoll and Y. C. Chang, Phys. Rev. B**40**, 9683 (1989); Phys. Rev. B**41**, 1447 (1989).
- ¹⁸ O. Madelung and M. Schulz, Landolt-Borstein (1982).
- ¹⁹ Mau-Phon Houng, Superlatt. Microstruct. **6**, 421 (1989).
- ²⁰ S. L. Chuang, Table III in Apendix.K, Physics of Optoelectronics Devices(John Wiley & Sons, Inc, 1995)
- ²¹ C. G. Vande Walle, Phys. Rev. B**39**, 1871 (1989).
- ²² G. D. Sanders and Y. C. Chang, Phys. Rev. B **31**, 6892 (1985).
- ²³ G. D. Sanders and Y. C. Chang, Phys. Rev. B**45**, 9202 (1992).

Figure Captions

Fig. 1. Schematic sketch of the QWR array fabricated in Refs. [1,2]. The QWR axis lies in the $[1\bar{1}0]$ direction. A and B label the Ga-rich and In-rich strips, respectively.

Fig. 2. Schematic diagram indicating the alignment between band edges of the constituent materials for QWR in case 1 (square profile) with and without the effect of strain. Solid lines are for unstrained bulk, dotted lines are for bulk under multi-axial strain appropriate for the present QWR, and dash-dotted lines are for $(50\text{\AA}/50\text{\AA})$ GaInAs/AlGaInAs superlattice including the multi-axial strain.

Fig. 3. Valance subband structures for QWR's with square profile for (a) Ga-composition $x = 0.6$ in Ga-rich and $x = 0.4$ in In-rich region and (b) $x = 0.7$ in Ga-rich and $x = 0.3$ in In-rich region.

Fig. 4. Valance subband structures for QWR's with sinusoidal profile with x ranging from x_m to $1 - x_m$ for (a) $x_m = 0.6$ and (b) $x_m = 0.7$.

Fig. 5. Squared optical matrix elements for transitions from HH1 and LH1 to the first conduction subband of the $(50\text{\AA}/50\text{\AA})$ $\text{Ga}_{0.7}\text{In}_{0.3}\text{As}/\text{Al}_{0.24}\text{Ga}_{0.24}\text{In}_{0.52}\text{As}$ superlattice for light polarized parallel (solid), perpendicular (dashed) to the QWR axis and z component (dotted).

Fig. 6. Squared optical matrix elements for transitions from the top three valance subbands to the first conduction subband for light polarized parallel (solid) and perpendicular (dashed) to the QWR axis for QWR's considered in Fig. 3.

Fig. 7. Squared optical matrix elements for transitions from the top three valance subbands to the first conduction subband for light polarized parallel (solid) and perpendicular (dashed) to the QWR axis for QWR's considered in Fig. 4.

Fig.1

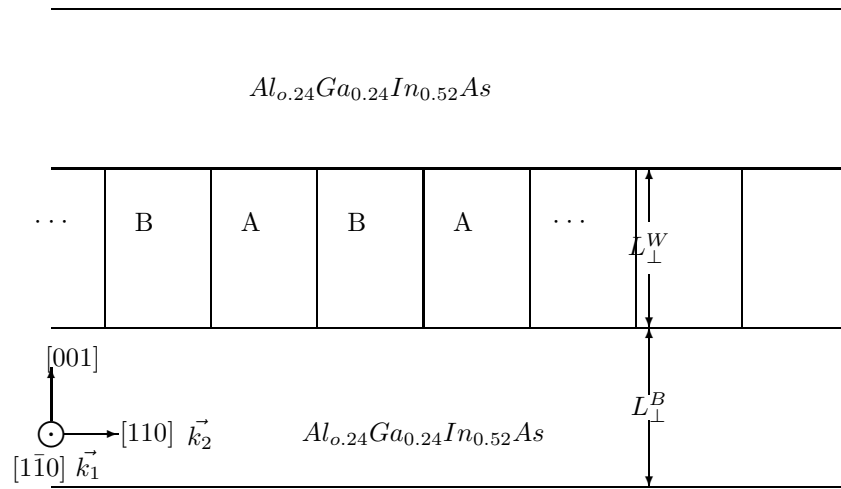
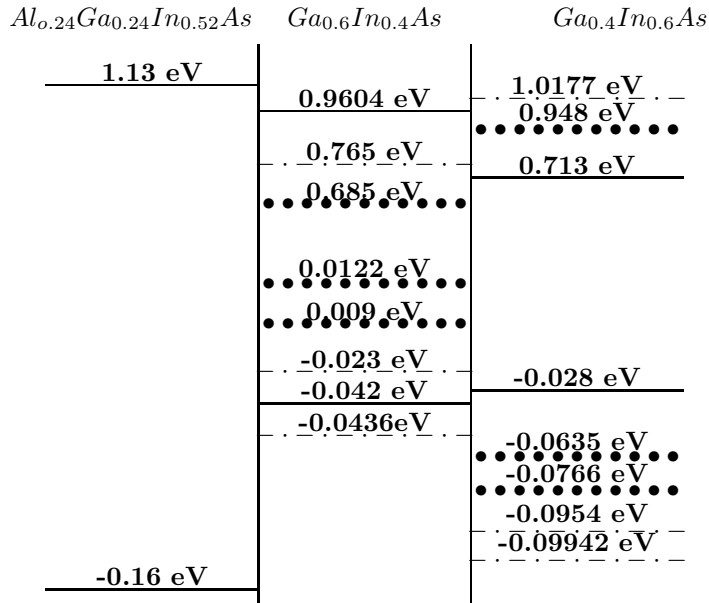


Fig.2

(a)



(b)

